Trans Indian Inst Met (2018) 71(8):2001–2013
https://doi.org/10.1007/s12666-018-1333-9

TECHNICAL PAPER

Study of the High Temperature Metallurgical Properties of On-Site Samples with Vanadium–Titanium Magnetite

Zhanwei He[1] · Hongrui Yue[1] · Xiangxin Xue[1]

Received: 31 August 2017 / Accepted: 13 April 2018 / Published online: 5 May 2018

Abstract In China, two typical vanadium–titanium magnetite ores were used as raw materials in iron making. In order to obtain the differences in the high temperature metallurgical properties of these ores, the phase and microstructure of on-site sinter, pellet, slag and laboratorial non-dripped slag were analyzed by XRD and SEM–EDS. The results show that the phases of two typical sinter and pellet have no significant changes, but the microstructures are different. The softening start temperature and softening zone of high chromium vanadium–titanium magnetite (HCVTM) burden are higher than ordinary vanadium–titanium magnetite (VTM) burden. The melting start temperature of HCVTM burden is higher and melting–dripping zone is smaller than VTM burden, which is beneficial to the blast furnace smelting. In addition, the calculation results using Factsage 7.0 are in accord with the experimental results. The primary crystal field of slag of HCVTM is the melilite, and the liquidus temperature is 1409.81 °C; the primary crystal field of slag of VTM is $CaTiO_3$, and the liquidus temperature is 1418.51 °C.

Keywords Vanadium–titanium magnetite · Blast furnace slag · Softening–melting–dripping behavior · Phase diagram

✉ Zhanwei He
hzw_413@sina.com

Hongrui Yue
1563570024@qq.com

Xiangxin Xue
xuexx@mail.neu.edu.cn

[1] School of Metallurgy, Institute of Resources and Environmental, Northeastern University, Shenyang, China

1 Introduction

Many important metallic resources, such as Fe, V and Ti, exist in vanadium–titanium magnetite ore [1, 2]. Such ore now constitute a hot spot in the study of smelting technology [3–7]. There are two typical vanadium–titanium magnetite ores in China: high chromium vanadium–titanium magnetite (HCVTM) and ordinary vanadium–titanium magnetite (VTM). HCVTM contains TiO_2 of 5.55% and Cr_2O_3 of 0.62%, while, TiO_2 content can reach 13% in VTM. HCVTM is mainly reserved in the Kuranakh deposit and used in Jianlong steel. However, VTM is mainly reserved in the Panzhihua mining area and used in Panzhihua steel. Compared to the ordinary iron ore, compositions of HCVTM and VTM are so complex that process of slagging and smelting in blast furnace is difficult. Currently the blast furnace process is the major method to extract valuable elements [1, 2]. In this process, most of iron and vanadium are reduced into hot metal, while almost all of Ti passes to the slag [2].

Over recent years, researches on the properties of sinter, pellet and slag with vanadium titanium magnetite have been conducted. Bristow et al. [8] showed that increasing the titanium magnetite levels to over 3% had a significant deterioration in sinter RDI. Liu et al. [9] studied reduction process of pellet containing high chromium vanadium titanium magnetite in cohesive zone. Cheng et al. [5] studied the effect of TiO_2 on the crushing strength for high chromium vanadium–titanium magnetite pellets. Qiu et al. [10] studied the effect of Cr_2O_3 addition on viscosity and structure of Ti-bearing blast furnace slag. In previous studies [8–15], researchers have altered some variables to find out how the modified sinter, pellet and slag would change under laboratory conditions. It was reported that the phase composition and microstructure of the laboratory and

Table 1 Chemical composition of vanadium–titanium magnetite

Component	Chemical composition (wt/%)								
	TFe	TiO_2	V	Cr_2O_3	FeO	SiO_2	Al_2O_3	MgO	CaO
HCVTM	60.93	5.55	0.561	0.62	31.28	1.47	3.33	1.06	0.15
VTM	54.45	13.10	0.34	0.01	31.89	3.25	3.78	2.72	1.09

Table 2 Chemical composition of on-site samples

Component	Chemical composition (wt/%)							
	TFe	TiO_2	V	Cr_2O_3	SiO_2	Al_2O_3	MgO	CaO
HCVTM								
Sinter1	46.98	1.63	0.20	0.25	5.40	1.91	3.04	16.28
Pellet1	60.83	3.69	0.36	0.39	6.37	2.48	2.06	0.58
Slag1	0.76	8.17	0.12	0.16	30.59	12.39	8.82	34.95
VTM								
Sinter2	50.20	7.88	0.21	0.11	5.71	3.17	2.57	9.99
Pellet2	53.41	9.90	0.29	0.22	6.11	3.55	2.50	1.91
Slag2	2.45	22.50	0.17	–	25.38	13.84	8.40	26.60

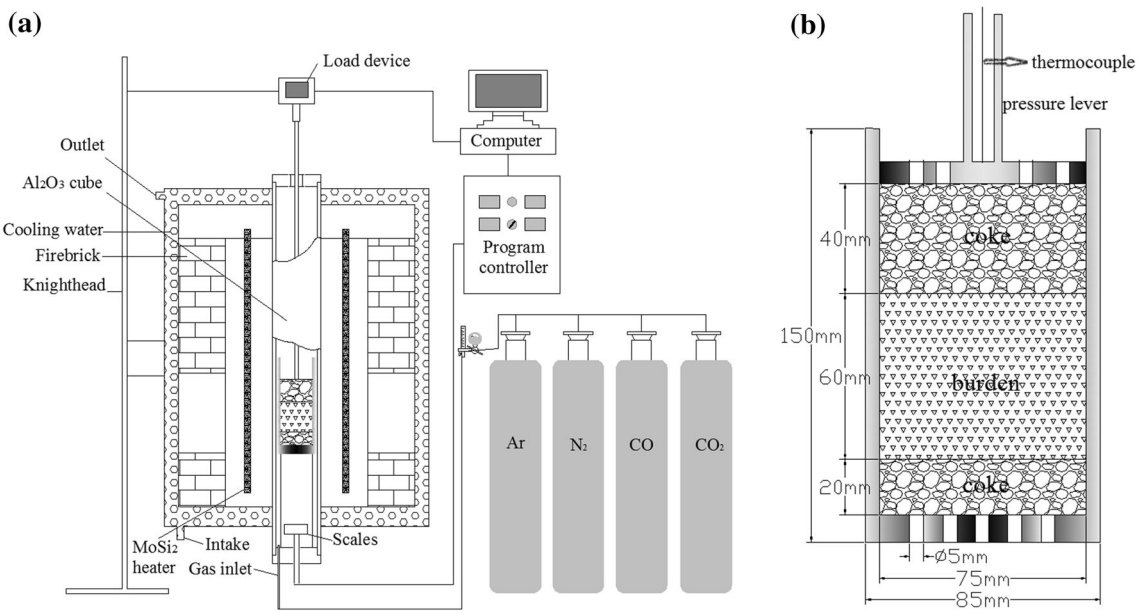

Fig. 1 Schematic of the experimental apparatus

on-site samples had definite differences [16, 17]. However, the on-site samples received little attention. So, the high temperature metallurgical properties of on-site sinter and pellet have been investigated in the laboratory. This article gives results about the phase composition and microstructure of on-site samples and non-dripped slag. The obtained results have been analyzed and compared with the phase diagram in the literature.

Table 3 The burden conditions of on-site sinter and pellet

	Sinter1	Siner2	Pellet1	Pellet2	Corrected TiO_2 (%)
Burden 1	300 g	–	200 g	–	2.45
Burden 2	–	431 g	–	69 g	8.16

Table 4 Temperature profile and reduction atmosphere of experiment

Temperature range	0–400 °C	400–900 °C	900–1020 °C	1020 °C to end
Heating-up rate	10 °C/min	10 °C/min	3 °C/min	5 °C/min
Heating-up time	40 min	50 min	40 min	>100 min
Gas composition	N2: 100 pct 3L/min	N_2: 60 pct 9L/min CO: 26 pct 3.9L/min CO_2: 14 pct 2.1L/min	N_2: 70 pct 10.5L/min CO: 30 pct 4.5L/min	

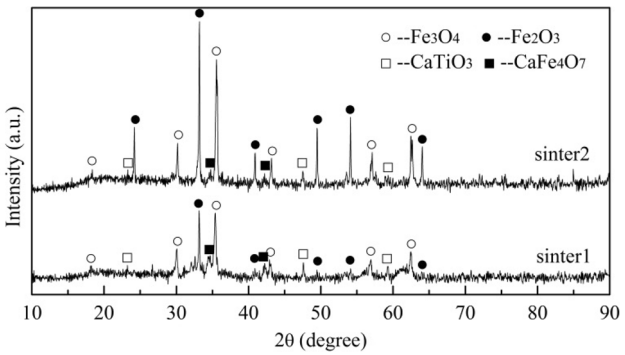

Fig. 2 XRD pattern of sinter1 and sinter2

2 Experimental

2.1 Sample Preparation

Table 1 shows that the chemical composition of vanadium–titanium magnetite. Sinter, pellet and slag, which were made of HCVTM (provided by Jianlong steel) or VTM (provided by Panzhihua steel), were taken out for future use, respectively, when the operation of the blast furnace was stabilized. The chemical compositions of the above samples were analyzed by chemical analysis. The chemical compositions of samples are shown in Table 2.

2.2 Procedure

In the present work, phase constitution and microstructure of the processed on-site samples were studied by X-Ray diffraction (XRD, model X'Pert Pro, Max power 3 kW, PANalytical B.V., Netherlands) and scanning electron microscope (SEM, model Ultra Plus, resolution ratio 0.8 nm, Carl Zeiss AG, Germany) analysis techniques. The softening–melting–dripping experiments of on-site samples were carried out to measure high temperature properties. The schematic experimental apparatus is shown in Fig. 1a. The device is mainly composed of heating system, gas control system, temperature control system, and data recording system. $MoSi_2$ heating elements were used as the core components in the heating system to heat and melt the burden. A R-type thermocouple was placed in the bottom of the pressure lever to control the experimental temperature. The crucible and pressure lever were both made of graphite. The dimension of the crucible is shown in Fig. 1b.

In order to simulate the blast furnace burden conditions, 500 g on-site sinter and pellet (as shown in Table 3) were put in the crucible and coke layers (size: 10–12.5 mm) of 20 and 40 mm height were placed below and over the samples, respectively. The displacement changes and contraction of the charging were measured by the displacement sensor when the experiment started. Experimental conditions are shown in Table 4. The heating rates were 10 °C/min below 900 °C, 3 °C/min at 900 °C to 1020 °C, and 5 °C from 1020 °C to the end. Ar gas was introduced immediately to prevent the dripped and non-dripped products being oxidized again after the reduction was finished.

3 Results and Discussion

3.1 Phase Constitution and Microstructure of Sinter and Pellet

Figure 2 shows the XRD pattern of sinter1 and sinter2 which are made from HCVTM and VTM, respectively. The main phase constitutions of sinter1 and sinter2 include

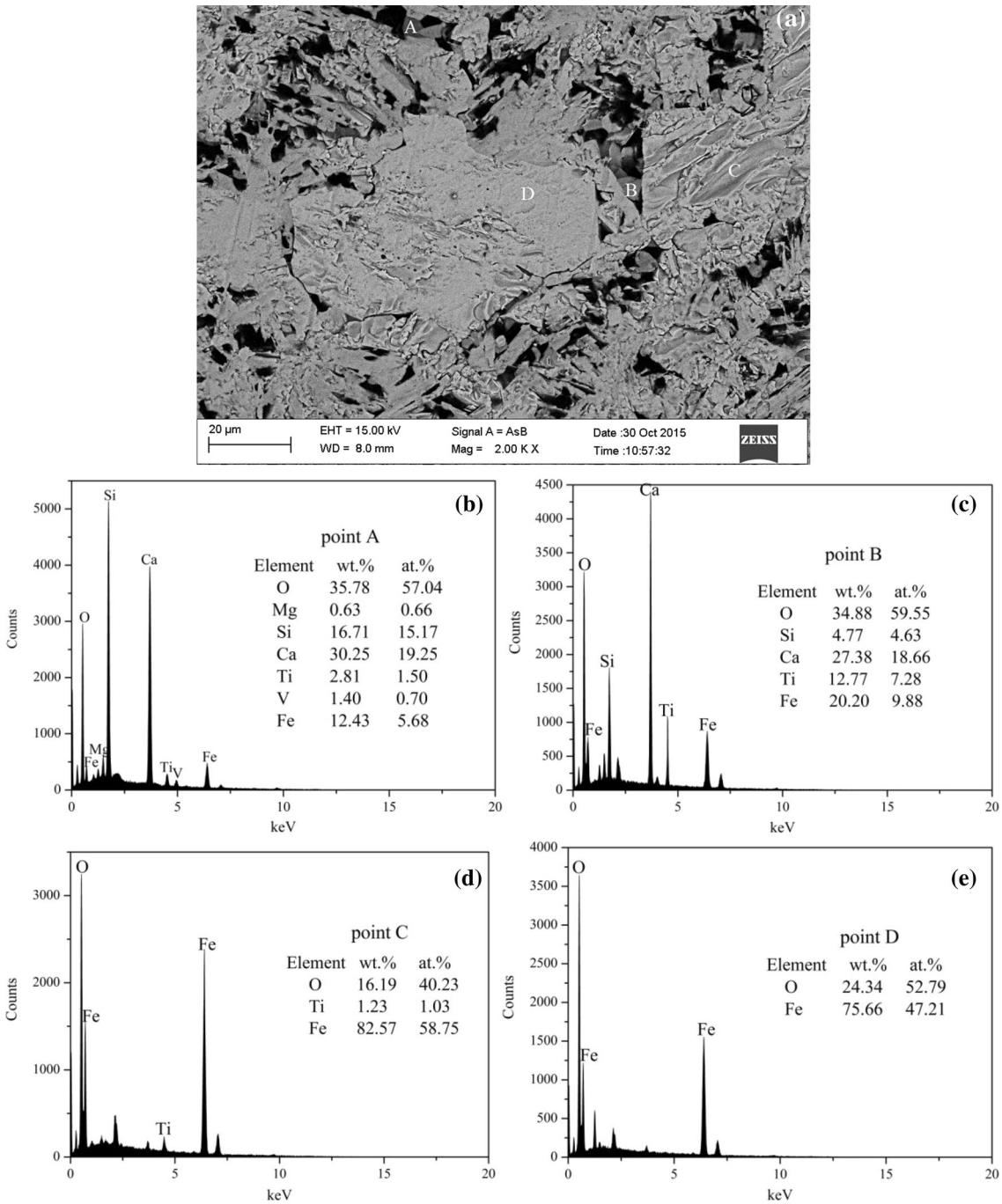

Fig. 3 SEM and EDS mapping analysis of sinter1

Fe_3O_4, Fe_2O_3, $CaTiO_3$ and $CaFe_4O_7$. The basic phases are Fe_3O_4 and Fe_2O_3, and the diffraction peak intensity of the basic phases in sinter2 is larger than sinter1. Whereas, the diffraction peak intensity of $CaTiO_3$ and $CaFe_4O_7$ in sinter2 is a bit less than sinter1.

Figures 3 and 4 show the SEM–EDS mapping analysis of sinter1 and sinter2, respectively. According to Fig. 3a, sinter1 is mainly composed of A, B, C and D-phase. From EDS results shown in Fig. 3b, it may be inferred that phase A is schorlomite. In Fig. 3c, point B contains an abundance of O and Ca and a small number of Si, Ti, Fe, which can be speculated as $CaO{\cdot}nFe_2O_3$ and $CaTiO_3$. Figures 3d, e show that the main elements are O and Fe, thus C-phase and D-phase may be Fe_2O_3 and Fe_3O_4 phase.

As shown in Fig. 4a, the main microstructure of sinter2 contains A, B, C and D-phase. Figure 4b shows that point A is composed of almost Fe and O, which can be inferred iron oxide phase (Fe_2O_3 and Fe_3O_4). Point B consists

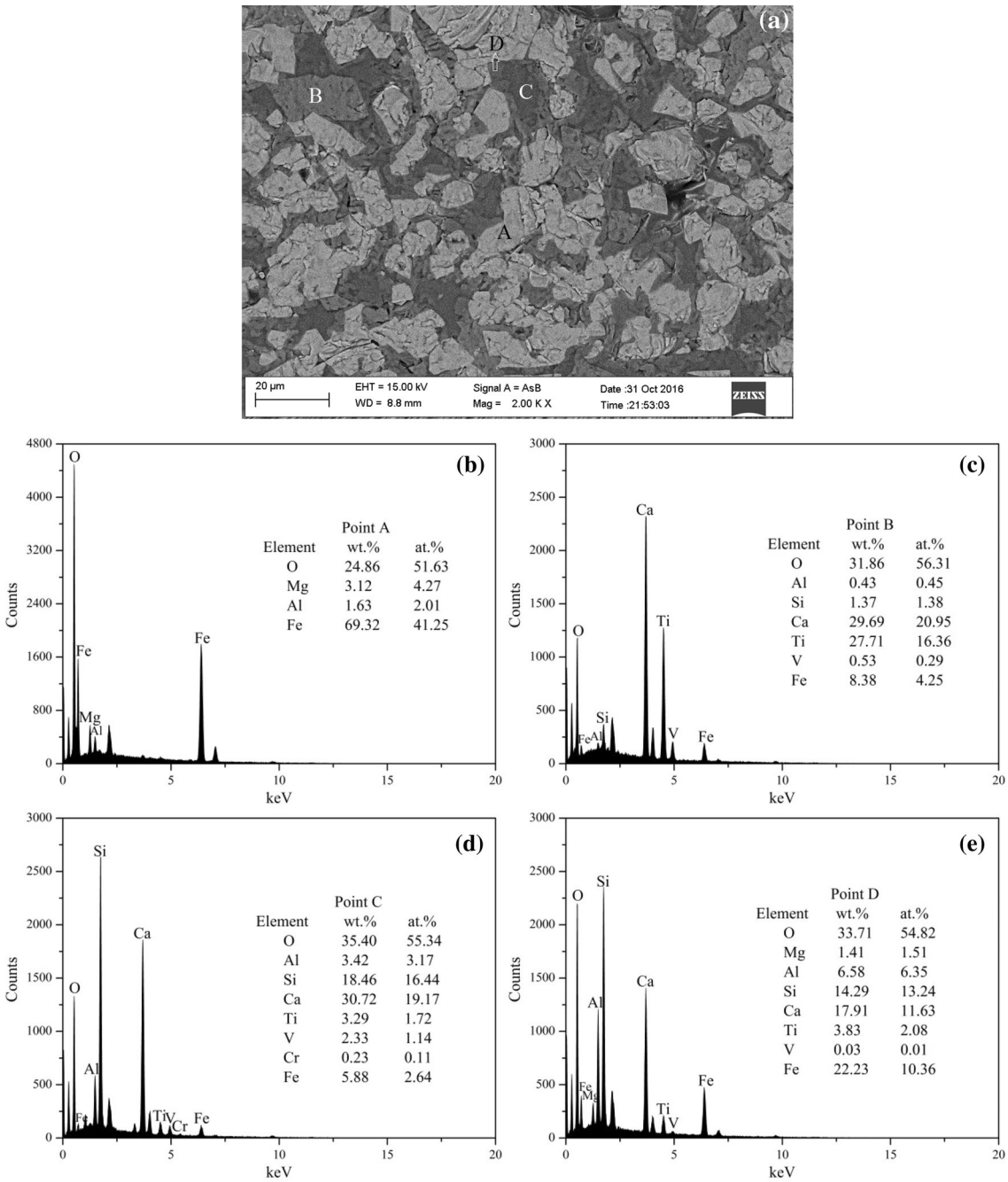

Fig. 4 SEM and EDS mapping analysis of sinter2

mainly of O, Ca, Ti and Fe in Fig. 4c, which can be inferred as $CaTiO_3$ and $CaO{\cdot}nFe_2O_3$. The main elements are O, Si, Ca and a little Al, Ti, V, Fe in Fig. 4d and e; thus C-phase and D-phase may be schorlomite. Because of the low melting point of schorlomite, the performance of sinter can be improved as binder phase. Comparing with Fig. 3, the microstructure of sinter2 contains much more binder phase. So, sinter2 is a more dense structure.

Figure 5 shows the XRD pattern of pellet1 and pellet2 made of HCVTM and VTM, respectively. The main phase compositions of pellet1 and pellet2 include Fe_2O_3, $MgTiO_3$ and $Fe_2O_3{\cdot}TiO_2$. In pellet2, the diffraction peak intensity of phase is a bit less than in pellet1.

Figures 6 and 7 show the SEM–EDS mapping analysis of pellet1 and pellet2, respectively. In Fig. 6a, the microstructure of pellet1 includes a lot of A-phase and a small amount of B, C and D-phase. In Fig. 6b, the main elements are O and Fe, thus A-phase could be Fe_2O_3. In Fig. 6c, point B contains mainly O, Ti and Fe, which can be inferred as $Fe_2O_3{\cdot}TiO_2$. In Fig. 6d, there is an

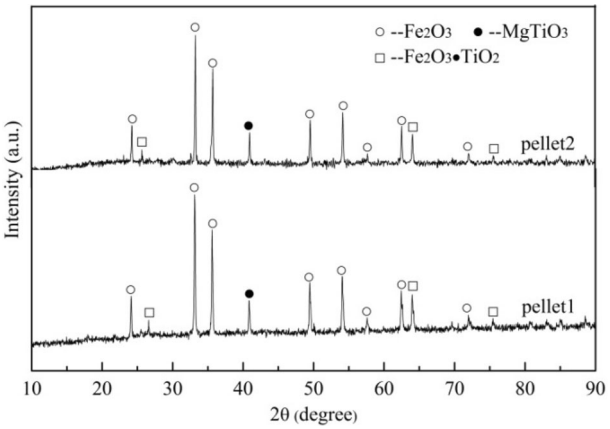

Fig. 5 XRD pattern of pellet1 and pellet2

abundance of O, Si and a small number of Al, Ca, Ti, V, Fe, which can be speculated as silicate mineral. The main elements are O and Ti in Fig. 6e, thus D-phase may be TiO_2.

As is depicted in Fig. 7a, pellet2 is mainly composed of A-phase. B-phase remains embedded in the A-phase, and C-phase is around A-phase. Figure 7b shows that point A includes mainly O and Fe, which could be Fe_2O_3. In Fig. 7c, the main elements are O, Ti and Fe, which can be inferred as $Fe_2O_3{\cdot}TiO_2$. There are lot of O, Si, Ca and a small amount of Mg, Al, Ti, V and Fe in Fig. 7d, thus point C may be silicate mineral.

The low melting point silicate mineral has grown due to interaction among particles at high temperatures. At the same time, the ilmenite of vanadium–titanium magnetite is oxidized to pseudobrookite ($Fe_2O_3{\cdot}TiO_2$) in pelletizing process, as seen in Eq. (1).

$$2FeO \cdot TiO_2 + \frac{1}{2}O_2 \rightarrow Fe_2O_3 \cdot TiO_2 \quad (1)$$

Taken together, mineralogical compounds of on-site sinter and pellet are listed in Table 5.

3.2 Softening–Melting–Dripping Behaviour

The inner shape of the cohesive zone of the blast furnace is determined by the melt-down of ores, and the permeability and distribution of gas there is also affected. Softening start temperature (T_4), softening temperature (T_{40}), melting start temperature (T_s), and dripping temperature (T_d) are measured to evaluate the softening and melting characteristics [18]. T_4 and T_{40} are the temperatures at which the contraction ratio of charging reaches 4 and 40%, respectively. The temperature accompanying differential pressure with a massive jumping is considered as T_s. The hot metal drips from the graphite crucible at a certain temperature as T_d. The results of softening and melting characteristics of burden are shown in Fig. 8.

Figure 8 shows that T_4, T_{40}, softening zone ($T_{40} - T_4$) of burden1 and burden2 are 1157, 1267, 110 °C and 1134, 1228, 94 °C, respectively. It can be seen that the softening property of burden1 is better than that of burden2. That is because a higher softening start temperature and a wider softening zone are favourable for the gas–solid reduction reaction in the blast furnace. Cheng et al.'s study [5] reports that T_4, T_{40} and ($T_{40} - T_4$) of pellet with 2.47 mass percent of TiO_2 are 1088, 1201 and 113 °C. Comparing with the previous results, it can be shown that T_4 of the burden1 with 2.45 mass percent of TiO_2 in this study is higher by 69 °C, T40 is higher by 66 °C, and ($T_{40} - T_4$) is higher by 3 °C. T_4 and T_{40} of burden1 are significantly higher than pellet with 2.47 mass pct TiO_2, but the difference of ($T_{40} - T_4$) is very small. Beside the TiO_2 difference, burden structure can also contribute immeasurably to the result change. It is also found that T_s, T_d and melting–dripping zone ($T_d - T_s$) of burden2 and bruden1 are 1246, 1480, 134 °C and 1205, 1490, 185 °C respectively. By the contrast analysis, melting start temperature of burden1 is higher and melting–dripping zone is narrower than burden2, which is beneficial to the blast furnace smelting.

The results of pressure drop and contraction of burden1 and burden2 are shown in Fig. 8. Permeability index (S) can be calculated by the equation $S = \int_{T_s}^{T_d} (P_m - \Delta P_s) \cdot dt$, where P_m is the pressure drop at any temperature and ΔP_s is the pressure drop at the T_s. The calculated S of burden1 and burden2 are 2426 and 2952 kPa °C, respectively. It can be seen that the permeability of burden2 is better than burden1.

In summary, the softening–melting–dripping property of burden1 with HCVTM is better than that of burden2 at a suitable ratio.

3.3 Non-Dripped Slag and On-Site Slag

The chemical compositions of non-dripped slag (ndslag1 and ndslag2) in the bottom of crucible at the end of dripping stage were analyzed by chemical analysis and are shown in Table 6.

Compared with Table 2, it is found that the mass percent of Fe in the non-dripped slag is significantly higher than on-site slag. It is necessary to analyze the phase constitution and microstructure of on-site slag and non-dripped slag.

Figure 9 shows the XRD pattern of on-site slag (slag1 and slag2) and non-dripped slag (ndslag1 and ndslag2), respectively. The main phase constitutions of ndslag1 and slag1 include $CaTiO_3$, melilite, $MgAl_2O_4$ and proxene. Ndslag2 and slag2 include $CaTiO_3$, $MgAl_2O_4$ and proxene. The diffraction peak intensity of $CaTiO_3$, proxene of ndslag2 and slag2 is larger than ndslag1 and slag1. In ndslag2 and slag2 the diffraction peak intensity of

$MgAl_2O_4$ is less than in ndslag1 and slag1. However, melilite does not appear in ndslag2 and slag2. It is also found that in the diffraction peak intensity of every phase, there exists difference between non-dripped slag and on-site slag.

Figure 10 shows SEM and EDS analysis of non-dripped slag1 (ndslag1) for HCVTM. It can be seen obviously from Fig. 10a that ndslag1 is mainly composed of A, B and C-phase. From Fig. 10b and c, A-phase is a complex silicate matrix phase, and B-phase remains embedded in A-phase as $CaTiO_3$.

Similarly, Fig. 11 presents on-site slag1 (slag1) for HCVTM at 2000×, together with the EDS analysis of A, B, C and D-phase. When compared with SEM and EDS analysis of non-dripped slag1, they all have silicate matrix and $CaTiO_3$ phase, but slag1 exists as $MgO{\cdot}Al_2O_3$ phase.

Figure 12 shows SEM and EDS analysis of non-dripped slag2 (ndslag2) for VTM. As is shown in Fig. 12a, ndslag2 is mainly composed of A, B, C, D and E-phase. It can be

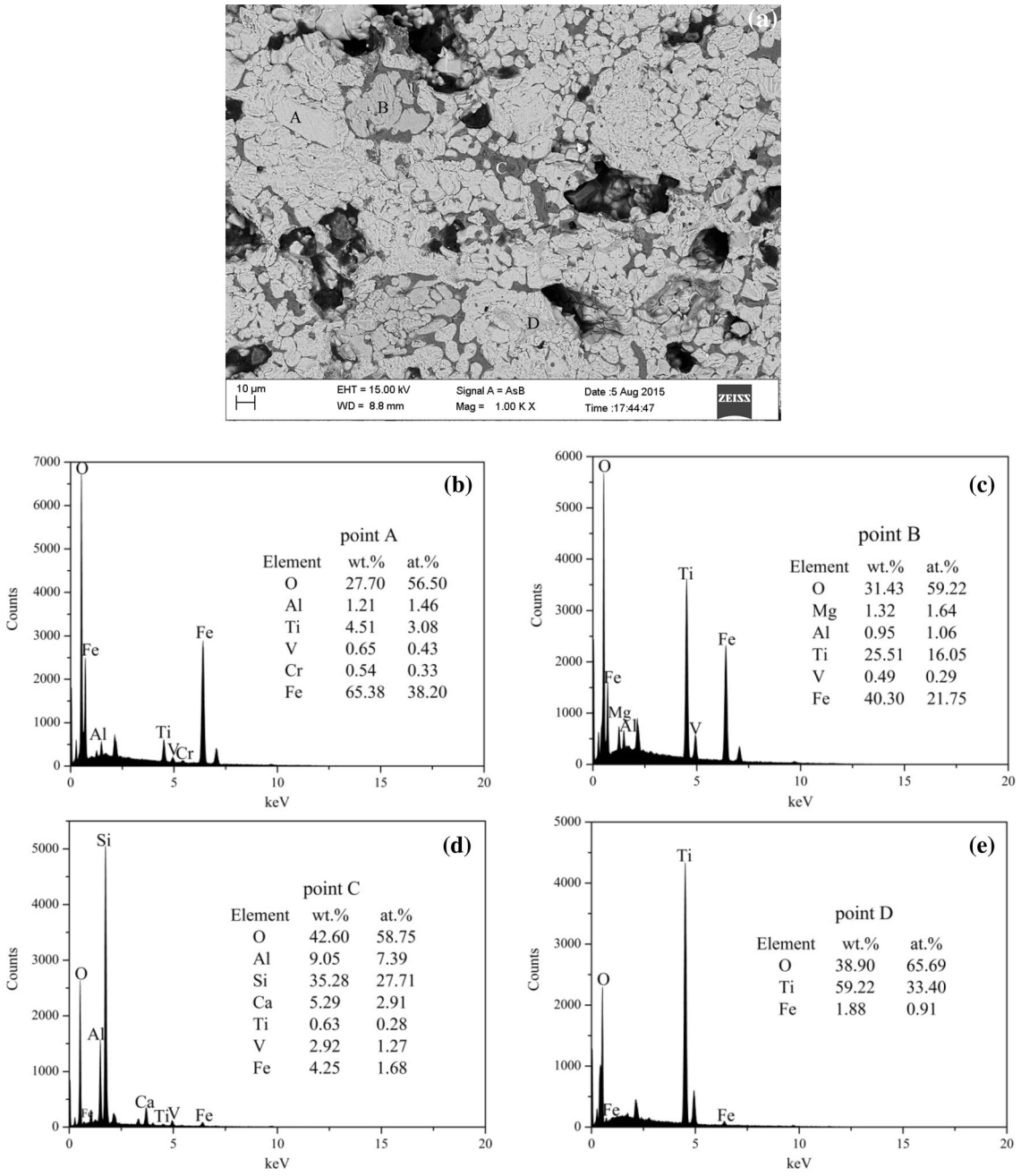

Fig. 6 SEM and EDS mapping analysis of pellet1

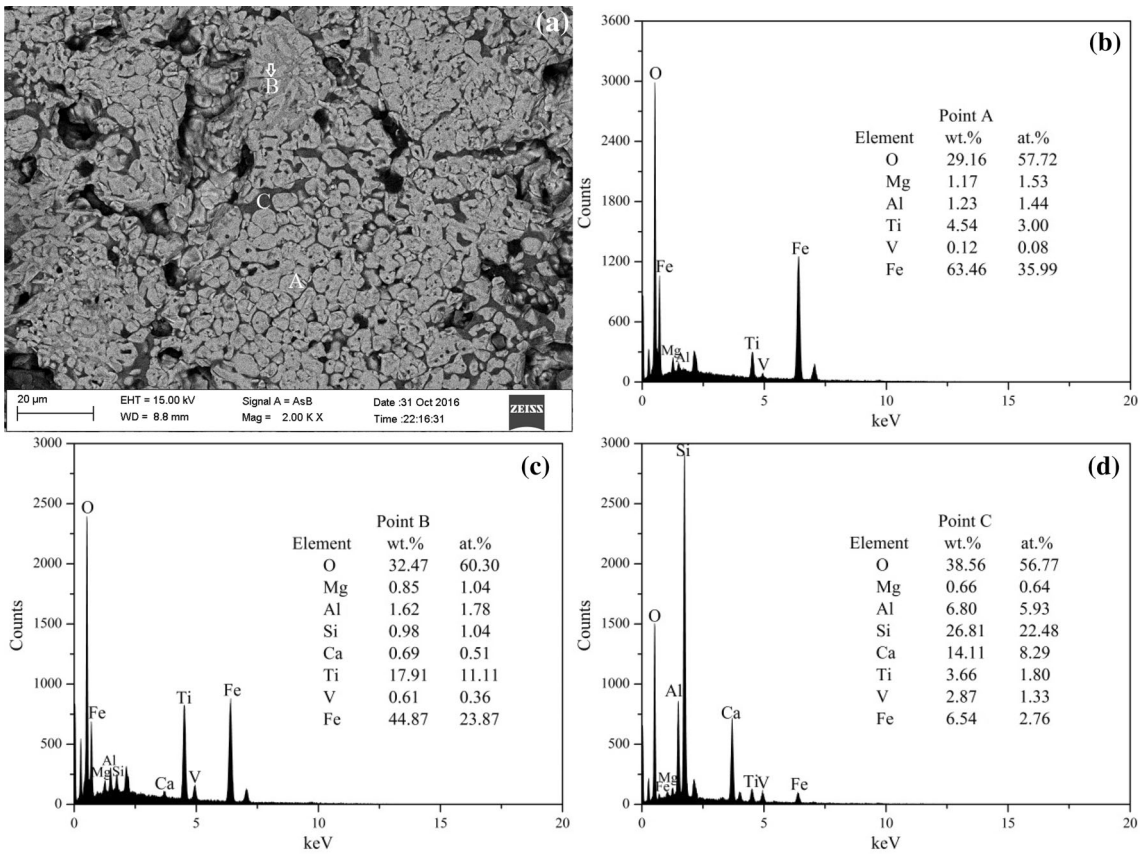

Fig. 7 SEM and EDS mapping analysis of pellet2

Table 5 Mineralogical compound of sinter and pellet

Component	Mineralogical compound
Sinter1	Fe_2O_3, Fe_3O_4, $CaTiO_3$, $CaO{\cdot}nFe_2O_3$, schorlonite
Sinter2	Fe_2O_3, Fe_3O_4, $CaTiO_3$, $CaO{\cdot}nFe_2O_3$, schorlonite
Pellet1	Fe_2O_3, $Fe_2O_3{\cdot}TiO_2$, TiO2, silicate mineral
Pellet2	Fe_2O_3, $Fe_2O_3{\cdot}TiO_2$, silicate mineral

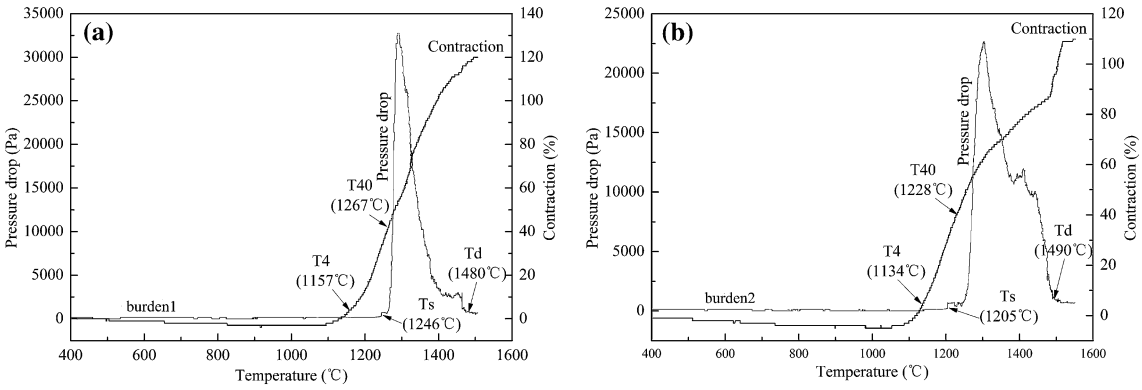

Fig. 8 The softening and melting characteristics of on-site sinter and pellet

Table 6 The chemical compositions of non-dripped slag

Component	Chemical composition (wt/%)							
	TFe	TiO_2	V	Cr_2O_3	SiO_2	Al_2O_3	MgO	CaO
Ndslag1	5.81	8.48	0.43	0.32	26.50	12.65	11.96	33.44
Ndslag2	4.20	19.67	0.18	0.03	24.63	12.48	7.12	31.25

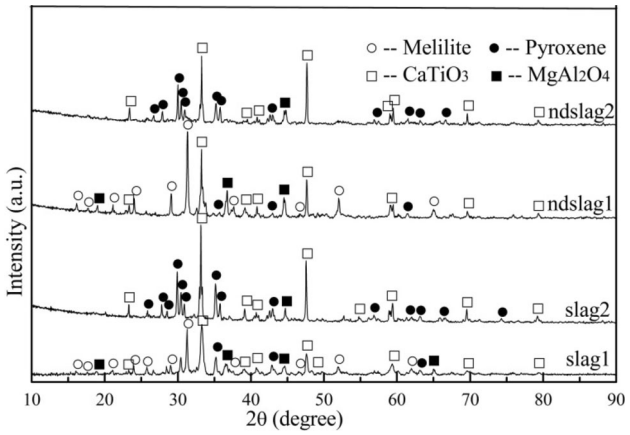

Fig. 9 XRD pattern of slag1, slag2, ndslag1 and ndslag2

inferred from Fig. 12b–e that point A and C are silicate matrix phase, and point B, D and E are $CaTiO_3$, metallic iron and TiC, respectively. It is proposed that TiC is generated through the reaction of Ti and C.

In a similar way, Fig. 13 presents on-site slag2 (slag2) for VTM at 1000×, together with the EDS analysis of A, B, C, D and E-phase. On the basis of Fig. 13a–f, point A is silicate matrix phase, and B, C and E are $CaTiO_3$, Fe_xO and metallic iron, respectively. When compared with SEM mapping of ndslag2, TiC does not appear in slag2. This is because non-dripped slag has been in a reducing atmosphere.

To explore the phase of slag, the Factsage 7.0 package was used to calculate the phase diagram. The V_2O_5 and Cr_2O_3 content were not considered in the calculations of

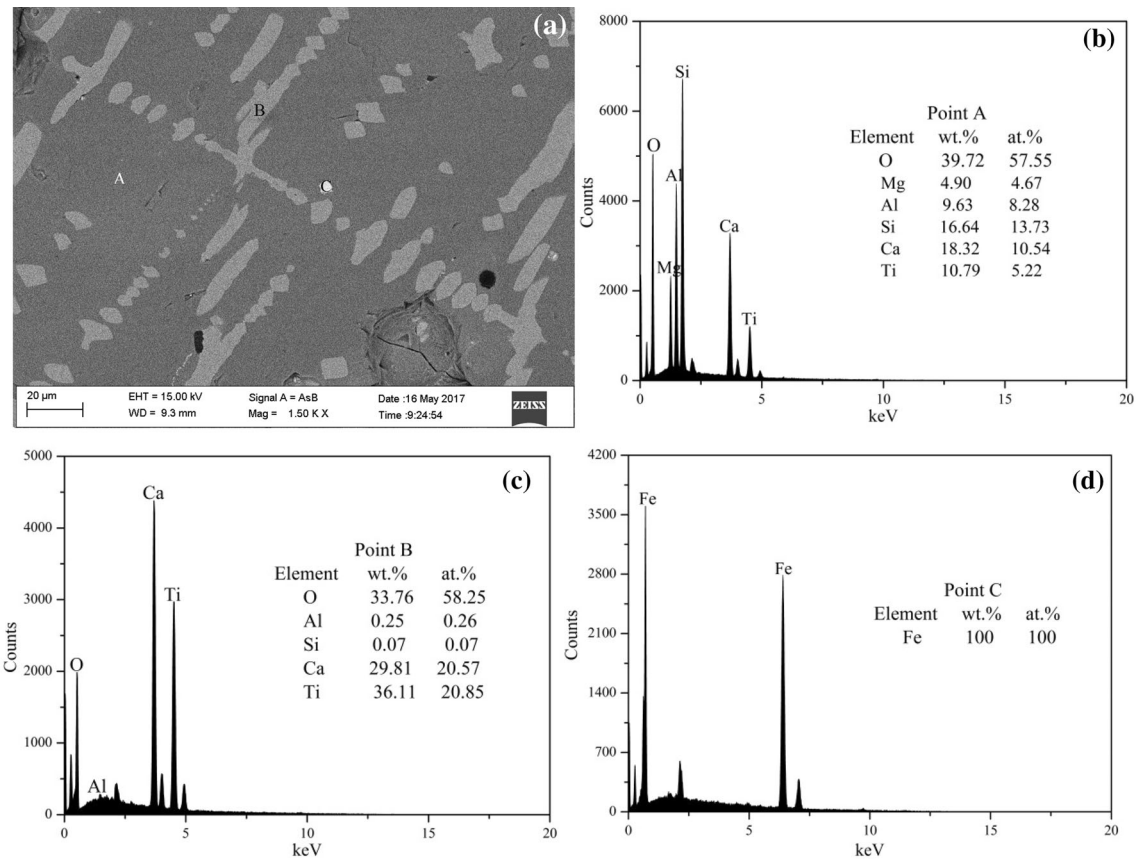

Fig. 10 SEM and EDS mapping analysis of ndslag1

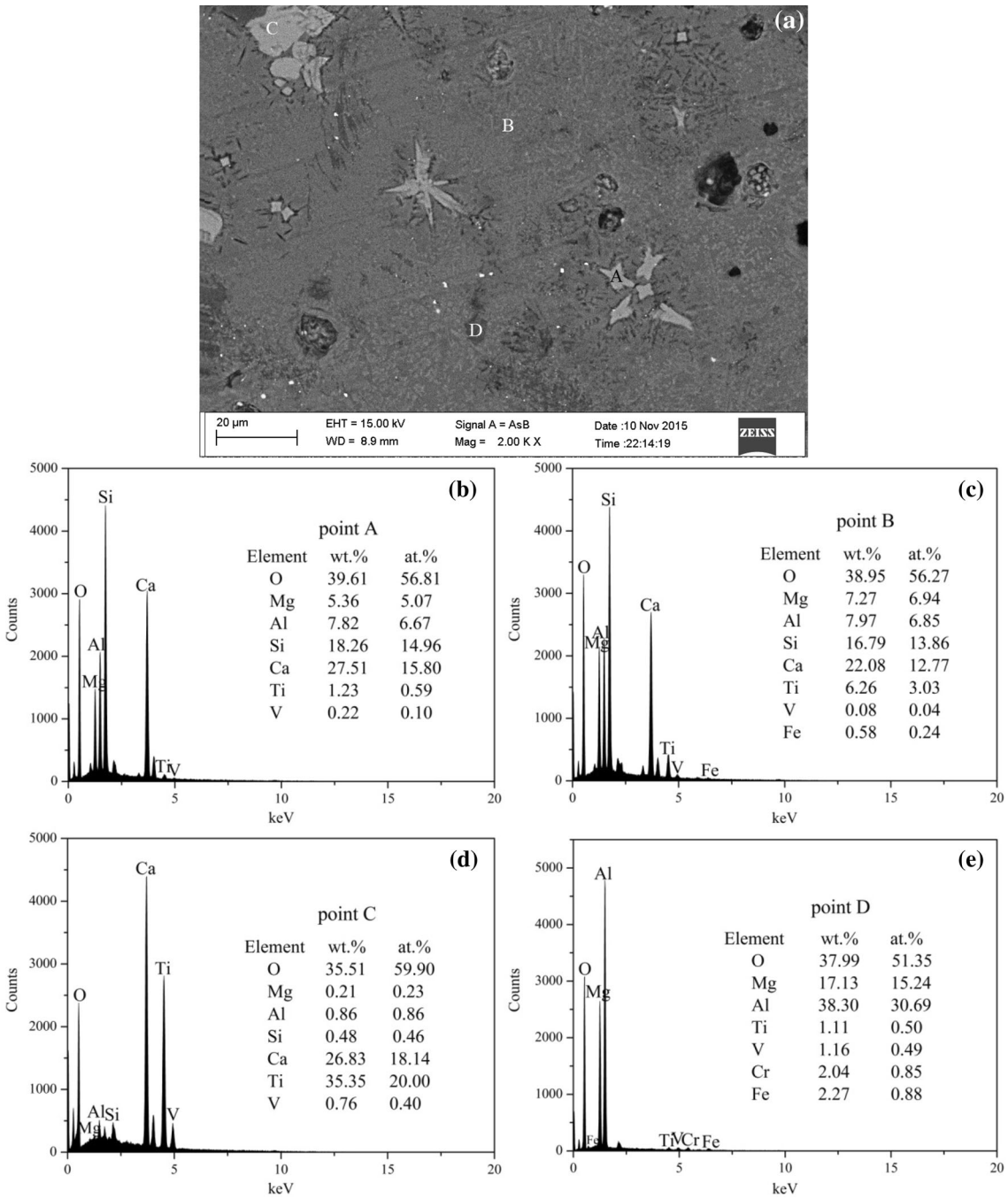

Fig. 11 SEM and EDS mapping analysis of slag1

the phase diagram as slag1 and slag2 contain small amount of V_2O_5 and Cr_2O_3. So the compositions of on-site slag were converted into CaO–SiO_2–TiO_2–Al_2O_3–MgO system, as shown in Table 7. The CaO–SiO_2–TiO_2–Al_2O_3–MgO system were calculated by Factsage 7.0 by setting an oxygen partial pressure by 10^{-5}. The FactPs and FToxid database were used, and the possible species of solid phases were considered, such as perovskite, melilite, spinel and so on. The phase diagram of CaO–SiO_2–TiO_2–13.05wt%Al_2O_3–9.29wt%MgO slag1 is shown in Fig. 14. The phase diagram of CaO–SiO_2–TiO_2–14.31wt%Al_2O_3–8.69wt%MgO slag2 is shown in Fig. 15.

As is shown in Fig. 14, the primary crystal field of slag1 with 8.61 wt% TiO_2 is melilite, and the liquidus temperature is 1409.81 °C. In Fig. 15, the primary crystal field of slag2 is $CaTiO_3$ when the content of TiO_2 is 23.26 wt%. At the same time, the liquidus temperature of slag2 is 1418.51 °C.

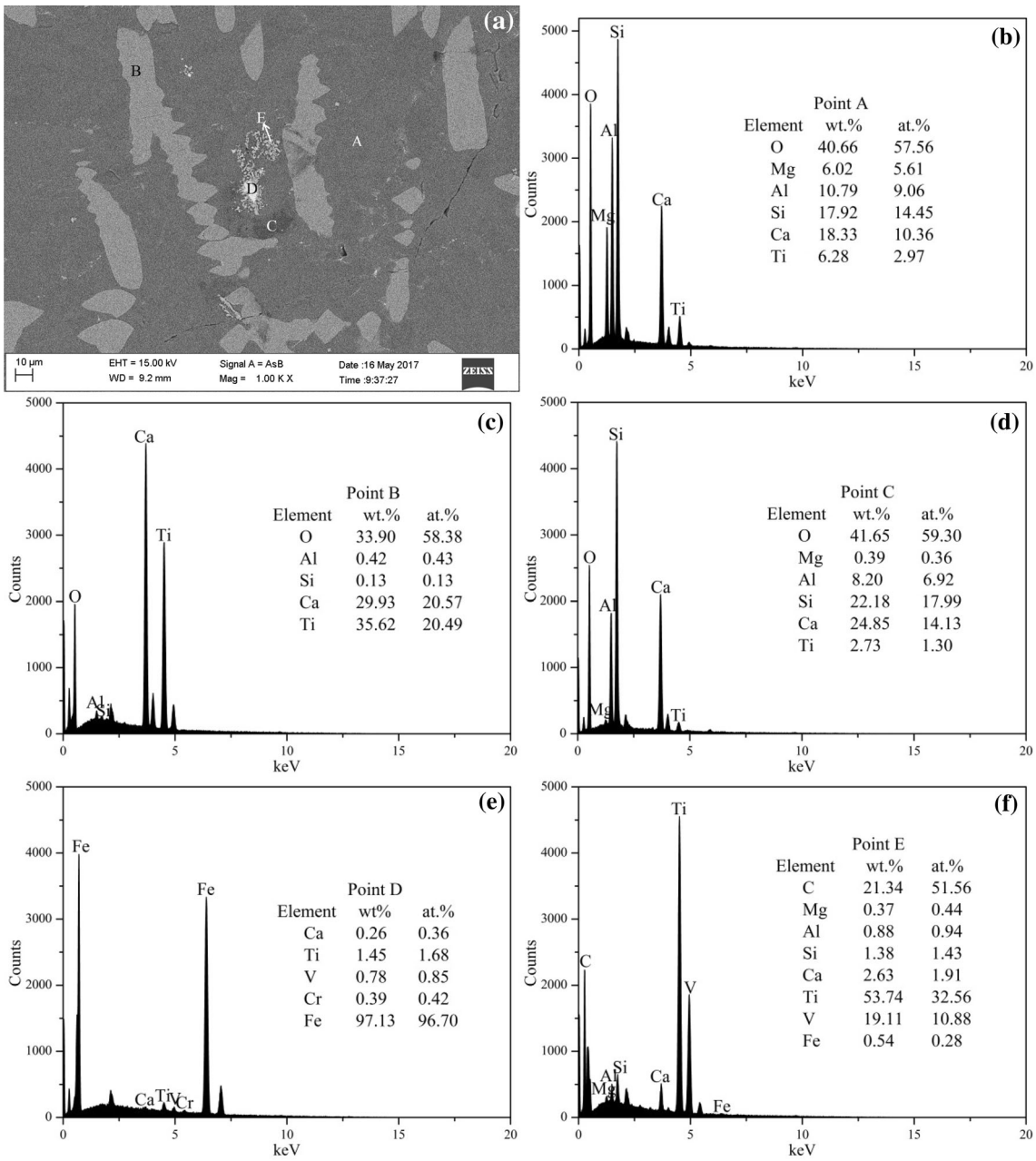

Fig. 12 SEM and EDS mapping analysis of ndslag2

4 Conclusions

In this study, the on-site sinter, pellet, slag and non-dripped slag which were made from HCVTM and VTM respectively were analyzed by XRD and SEM–EDS. The high temperature metallurgical properties of on-site sinter and pellet were investigated. Besides, the target slag was discussed by phase diagram. The conclusions are as follows:

(1) The phases of HCVTM and VTM sinter contain Fe_2O_3, Fe_3O_4, $CaTiO_3$, $CaO{\cdot}nFe_2O_3$, schorlonite; the phases of HCVTM pellet contain Fe_2O_3, $Fe_2O_3{\cdot}TiO_2$, TiO_2, silicate mineral, and the phases of VTM pellet contain Fe_2O_3, $Fe_2O_3{\cdot}TiO_2$, silicate mineral.

(2) The softening start temperature and softening zone of HCVTM burden are higher than VTM burden; the melting start temperature of HCVTM burden is higher and melting–dripping zone is smaller than VTM burden, which is beneficial to the blast furnace smelting.

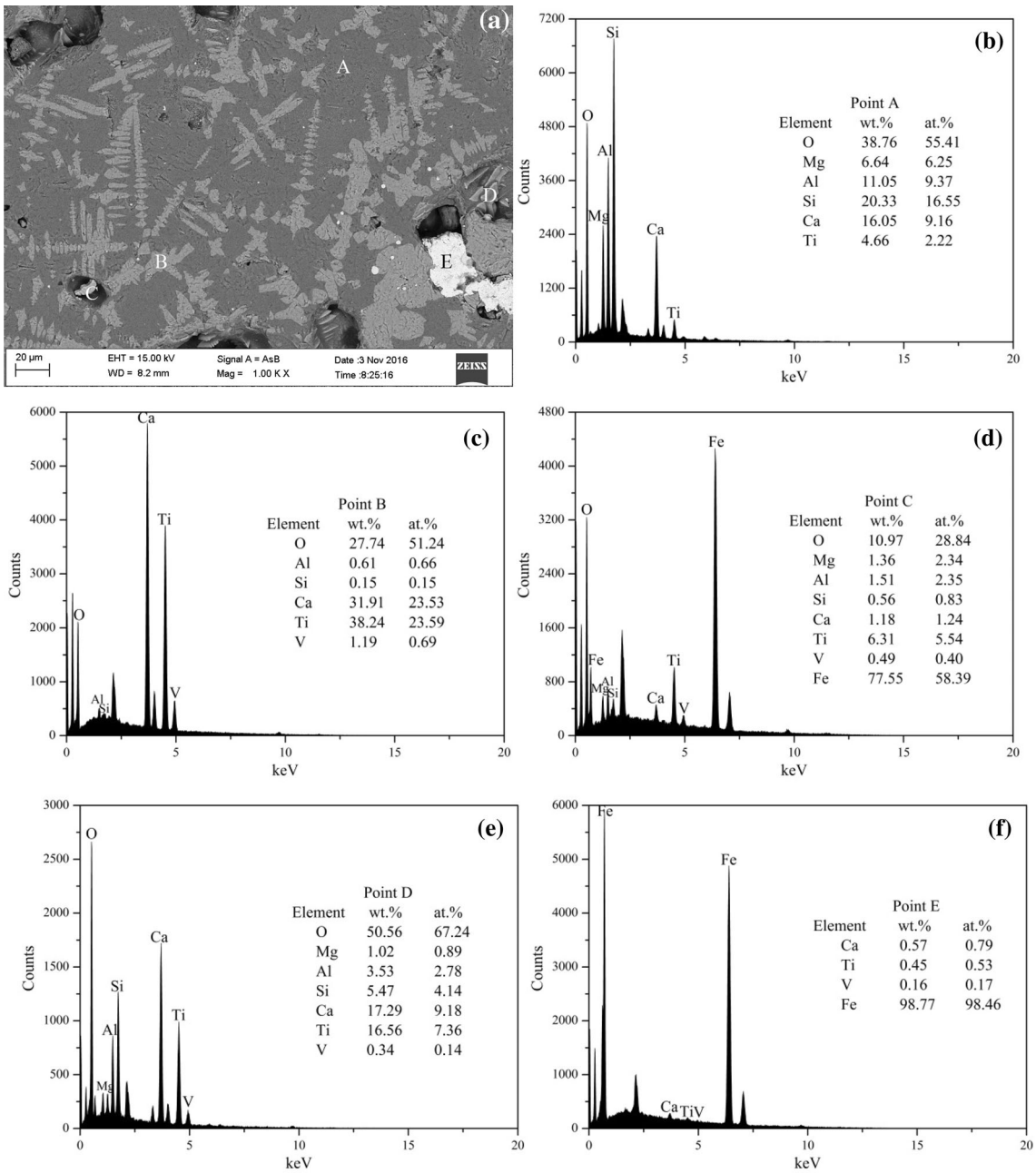

Fig. 13 SEM and EDS mapping analysis of slag2

Table 7 Oxide composition of target slag

No.	Target slag composition					
	CaO	SiO_2	TiO_2	Al_2O_3	MgO	CaO/SiO_2
TS1	36.82	32.23	8.61	13.05	9.29	1.14
TS2	27.50	26.24	23.26	14.31	8.69	1.05

(3) The phase constitutions of on-site slag are not different from laboratorial slag, but there are some differences in the microstructure. The laboratorial VTM slag shows obviously TiC around metallic iron.

(4) The main phase and primary crystal field of slag1 is the melilite, and the liquidus temperature is 1409.81 °C; the main phase and primary crystal field

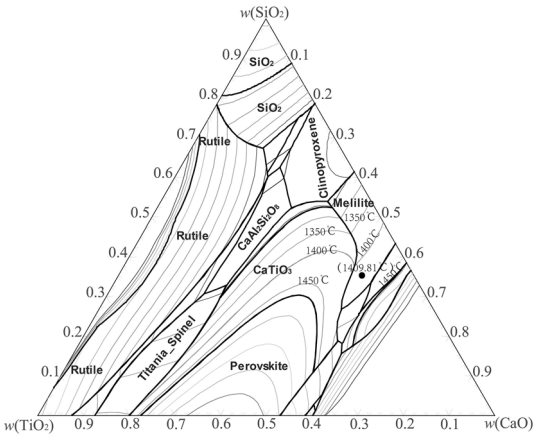

Fig. 14 Phase diagram of CaO-SiO_2-TiO_2-13.05wt%Al_2O_3-9.29wt%MgO slag

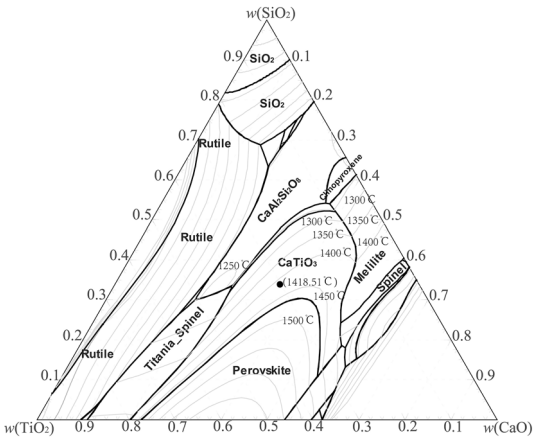

Fig. 15 Phase diagram of CaO-SiO_2-TiO_2-14.31wt%Al_2O_3-8.69wt%MgO slag

of slag2 is $CaTiO_3$, and the liquidus temperature is 1418.51 °C.

Acknowledgements This work was supported by the National Project Support Program of China under Grant number 2015BAB19B02; 973 Program under Grant number 2013CB632603.

References

1. Du H G, *The blast furnace smelting principle of vanadium–titanium magnetite*, Science Press, Beijing (1996).
2. Wang X Q, *Smelting vanadium titanium magnetite with blast furnace*, Metallurgical Industry Press, Beijing (1994).
3. Li W, Fu G Q, Chu M S, and Zhu M Y, *Ironmak. Steelmak.* **44** (2017) 294.
4. Zhou L H, and Zeng F H, *Ironmak. steelmak.* **38** (2011) 59.
5. Cheng G J, Xue X X, Jiang T, and Duan P N, *Metall. Mater. Trans.* B **47** (2016) 1713.
6. Cheng G J, Liu J X, Chu M S, and Xue XX, *Ironmak. Steelmak.* **42** (2015) 17.
7. Zhang K, Zhang Z T, Liu L L, and Wang X D, *Metall. Mater. Trans. B* **45** (2014) 1389.
8. Bristow J, and Loo C E, *ISIJ Int.* **32** (1992) 819.
9. Liu J X, Cheng G J, Liu Z G, Chu M S, and Xue X X, *Steel res.* **86** (2015) 808.
10. Qiu G B, Chen L, Zhu J Y, Lv X W, and Bai C G, *ISIJ Int.* **55** (2015) 1367.
11. Dong X J, Sun H Y, She X F, Xue Q G, and Wang J S, *Ironmak. Steelmak.* **41** (2014) 99.
12. Guo Y-F, Zhou J-F, Jiang T, Chen F, Song X-L, Tang M-J, and Qing L-J, in: 4th International Symposium on High-Temperature Metallurgical Processing, TMS, San Antonio, Texas, USA (2013), 509.
13. Ostrovskin O, *ISIJ Int.* **44** (2004) 74.
14. Shen F M, Gao Q J, Wei G, Jiang X, and Shen Y S, *Steel Res. Int.* **86** (2015) 644.
15. Liao J L, Li J, Wang X D, and Zhang Z T, *Ironmak. Steelmak.* **39** (2012) 133.
16. Wu L S, Gran J, and Du S C, Metall. *Mater. Trans.* B **42** (2011) 928.
17. Hao J L, *Influence of MgO/Al_2O_3 on properties of BF slag in Nanjing iron & steel Co., Ltd*, M.S. Thesis, Chongqing University (2014).
18. Chu M S, *Raw fuels and auxiliary materials in ferrous metallurgy.* Metallurgical Industry Press, Beijing (2010).